COBEM 2023 27TH INTERNATIONAL CONGRESS OF MECHANICAL ENGINEERING

ABCM Brazilian Society of Mechanical Sciences and Engineering
27th ABCM International Congress of Mechanical Engineering
December 04-08, 2023, Florianópolis-SC, Brazil

COB-2023-XXXX
DIFFICULTIES AND BENEFITS OF MODELLING THE ACHILLES TENDON USING FEM

Otávio Teixeira Pinto
Bruno Klahr
José Luís Medeiros Thiesen
Eduardo Alberto Fancello
Federal University of Santa Catarina, Florianópolis, SC, Brazil
otaviotpinto@yahoo.com.br, bruno.klahr@posgrad.ufsc.br, joselmthiesen@gmail.com, eduardo.fancello@ufsc.br
Thiago André Carniel
Community University of Chapecó Region, Chapecó, SC, Brazil
thiago.carniel@unochapeco.edu.br

Abstract. *The Achilles tendon is made of three subtendons. The proper inclusion of the mechanics of the mesostructure of these three subtendons and the force transference among them is decisive to represent the non uniformity in the stress and strain fields. Such non uniformity can be the cause of abnormalities such as: tendinopathies, calcifications, presence of scar tissue and calcifications. Understanding of the precise level of impact of such abnormalities in the mechanical behavior of the Achilles tendon could influence the decision making process of physiotherapists, physicians and physical education professionals and for that goal a computational model of the Achilles tendon is proposed. The model represents the tendon as an elliptical cylinder where the magnitude of the two semi-axis of the ellipse vary as a function of the axial cross section position. Internally the mesostructure was represented as a division of the domain in four parts: the three subtendons and an interface of finite thickness separating the subtendons. The subtendons twist around the cylinder axis. A transversely isotropic hyperelastic material model was used to represent the subtendon material. Two different levels of subtendon twist and three different levels of shear resistance for the interface were compared with each other and with experiments from the literature. Nine different sets of boundary conditions were tested for each model in order to properly represent the experiments. The difficulties and potential benefits of the model are discussed.*

Keywords: *Achilles tendon, FEM, Soft Tissues, Hyperelastic, Anisotropic*

1. INTRODUCTION

The Achilles tendon is the strongest tendon in the human body and one of the most important for human locomotion (Yin *et al.*, 2021a). For this reason, any rupture, tendinopathy or pain in it can hinder our ability to stand, walk, run or jump, affecting lifestyle, autonomy, work and even ending the careers of some professions such as manual workers, soldiers, dancers and athletes. To understand the Achilles tendon, it is important to realize that: 1) it is not a homogeneous structure, 2) it is not submitted to homogeneous loads or stimuli and 3) it exhibits great variation in shape and mechanical behaviour among subjects.

1.1 Description of the Achilles tendon, muscles and anatomy/morphology

The Achilles tendon is the distal portion of the triceps surae muscle-tendon unit (MTU). Its distal extremity inserts in the posterior portion of the calcaneus forming a contact region (enthesis) that is not perpendicular to the fibers of the tendon. Its proximal extremity is connected indirectly to the three heads of the triceps surrae by three aponeurosis (one for each head of the triceps surrae (Edama *et al.*, 2015)).

The triceps surrae is formed by three muscles, the lateral gastrocnemius muscle, the medial gastrocnemius muscle and the soleus muscle. The soleus muscle originates from the proximal and posterior portions of the tibia and fibula (*i.e.* Distal to the knee joint). The lateral and medial gastrocnemius originate from the lateral and medial condyles of the femur respectivelly (*i.e.* Proximal to the knee joint). The gastrocnemius muscles span across three joints from their origin to their insertion: the knee joint, the talocrural joint, and the subtalar joint. The soleus muscle crosses only the last two. The main movements of the knee joint is the flexion and extension, which makes the gastrocnemius shorten or lengthen respectively. The main movement of the talocural joint is the plantarflexion and dorsiflexion of the ankle, which makes the whole MTU shorten or lengthen. The main movement of the subtalar joint is the inversion and eversion of the ankle, which produces a rotation in the the distal portion of the Achilles tendon around a sagittal axis passing through the center of rotation of the joint. The position of the femur, tibia, fibula, talus and calcaneus bones determines the position of the

triceps surrae MTU extremities in space at a given time (Figure 1).

Figure 1: Visualization of the origin and insertion of the triceps surae MTU in the left leg. Blue represents the origin of the lateral gastrocnemius muscle, red represents the origin of the medial gastrocnemius muscle, yellow represents the origin of the soleus muscle and green represents the Achilles tendon insertion.

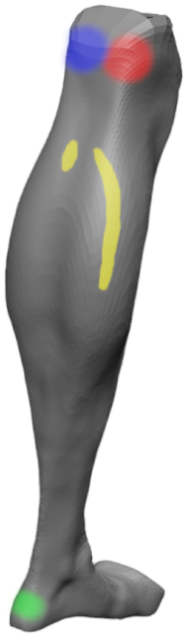

Internally the Achilles tendon fibers are segregated to the point that they can be separated by dissection (Edama *et al.*, 2016). Such separated regions are known to twist along the AT axis in a rope-like fashion. The twist occur as a right-hand thread in the left leg and as a left-hand thread in the right leg. The degree of twist can vary among subjects and among the legs of the same subject (Edama *et al.*, 2016; Benjamin *et al.*, 2007).

When the three aponeurosis cross the myotendinous junction, their shape becomes thicker and less wide transitioning from the shape of an aponeurosis to the shape of a tendon. It is then more appropriate to call each of then a subtendon. Each subtendon is attached to a different muscle of the triceps surae and could be under loads or elongations that are different from the other two subtendons. This is specially true when we are comparing a subtendon of the gastrocnemius muscles to the subtendon of the soleus muscle. However, because they are twisted and the lateral force transference is non negligible (non negligible shear stresses) it is observed a non negligible influence of a given subtendon on its neighbors. This lateral force transference tends to be less present in young subjects and more present in old subjects and such correlation with age is associated with the well know phenomena of adhesion associated with the accumulation of advanced glycation end products (Yin *et al.*, 2021a; Pekala *et al.*, 2017; Handsfield *et al.*, 2017)

Such sliding occur in the interface among the subtendons. Such interface is usually represented as a contact interaction in finite element models of the Achiles tendon (Yin *et al.*, 2021a; Shim *et al.*, 2018). Despite its small thickness, the interface is used as a guide in dissections aimed at separating the subtendons (Prosenz *et al.*, 2018), and its thickness can be seen on magnetic resonance imaging (Szaro *et al.*, 2020). However, to our knowledge, its mean thickness has not been reported.

1.2 Heterogeneous strains in tendons are associated with tendinopaties

It has been reported that the presence of heterogeneous strains in the Achilles tendon can cause tendinopathies **(Reference).**. Some subjects present stress shielded regions inside their Achilles tendon. The stress shielding leads to a local tissue adaptation for the lack of load or even for the presence of compressive loads, forming cartilage-like changes (Maganaris *et al.*, 2004). Such compression loads were observed in experiments with human Achilles tendons *in vitro* (Lersch *et al.*, 2012). Similarly, non-uniform strains pattern were observed *in vivo* (Bogaerts *et al.*, 2017), and by computational simulations (Shim *et al.*, 2018). The shielded region could then eventually go under high levels of tension due to a sport related gesture and injuries may occur. This etiological pathway shows a paradoxical relationship where some lesions that are thought to be caused by overuse are actually caused by underuse (Maganaris *et al.*, 2004). The contrary is also true. Tendinopathies can cause inhomogeneities in the strain field. Aging is known to affect sliding capabilities (Yin *et al.*, 2021a) as a consequence the tendon behaves less as a bundle of independent fibers and more like a beam (i.e. with non-negligible resistance to bending). Beam-like behaviour was observed in older subjects (Lersch *et al.*, 2012) where the strain field had regions less stressed than others due to the rotation of one of its ends. Similarly, calcific tendinopathy and

insertional calcific tendinopathy are localized deposits of calcium in the substance of the tendon. Such deposits are known to add stifness to the tissue and, as a consequence, changes in the strain field near them (Oliva *et al.*, 2012). The response of the body includes surrounding the deposits with cartilage like material (Oliva *et al.*, 2012), a probable adaptation to the compressive stresses that typically are present around a stiff inclusion in soft materials under tension.

1.3 Motivation and Justification of this work

The finite element method (FEM) has already been used to model the Achilles tendon.

Yin *et al.* (2021b) used a series of photographs taken from dissected Achilles tendons to create a FEM model that takes into account the actual geometry of the tendon and its subtendons. They used multiple photographs of the cross section of dissected human Achilles tendons as reference. Similarly, Obrezkov *et al.* (2022) based their geometry in images from tendon cross sections and took into account the actual geometry of the tendon and its subtendons. However, Obrezkov *et al.* (2022) did not define their cross sections based on multiple images, but rather used one of the cross sections presented in Edama *et al.* (2015) as reference and built all the geometry based on it. Diniz *et al.* (2023) also based their geometry in images, but in their case they used MRI images from live subjects. The subtendon twisting, however, was not obtained from the images, but added afterwards by proposing two different levels of twisting based on the findings of Edama *et al.* (2015). Finally, Shim *et al.* (2014, 2018, 2019) also based their geometry in medical images and take into consideration the subtendon twisting.

All this propositions have in common the fact that they use a geometry that, to some degree, captures the tortuosity of the Achilles tendon geometry. All works cited above inserted in their geometries the general external silhouette of the Achilles tendon with its misalignments and even some of its topography.

In this work, a different approach is proposed. The geometry is fully parametrized as a series of parallel and concentric ellipses spaced from each other. This approach was chosen as a way to avoid the presence of misalignments and misinterpretation of the numerical results of the finite element analysis with minimal influence of artifacts on the simulation fields..

2. Method

2.1 Model geometry

The geometry of the tendon has been idealized as a set of elliptical sections parallel to the transverse plane of the body and connected by their center to the tendon axis. Such axis was defined as the straight line passing through the geometrical center of the tendon and parallel to its longest dimension. The distal most portion of the geometry was defined as the origin (Figures 2 and 3).

Each ellipse has one of its principal axis parallel to the frontal plane (medial-lateral aspect) and the other parallel to the median plane (anterior-posterior aspect). The dimensions of each transversal section follow the spline curves that approximate the measurements obtained in Obst *et al.* (2014). The spline curves used to define the ellipses are shown in Figure 2, which represent the MLR (Medial Lateral Radius) and APR (Anterior Posterior Radius) measurements. Extra points were added to represent a transition region portion proximal to the soleus myotendinous junction (MTJ).

Figure 2: Representation of the ellipsoidal cross sections and the curves used as guide for the principal axis of each ellipse. Achilles tendon cross section medial-lateral radius (MLR). Achilles tendon cross section anterior-posterior radius (APR). From z=0 to z=60 (green dashed line) the curves were based on experimental data from Obst *et al.* (2014). From z=60 to z=120 the curves were extrapolated.

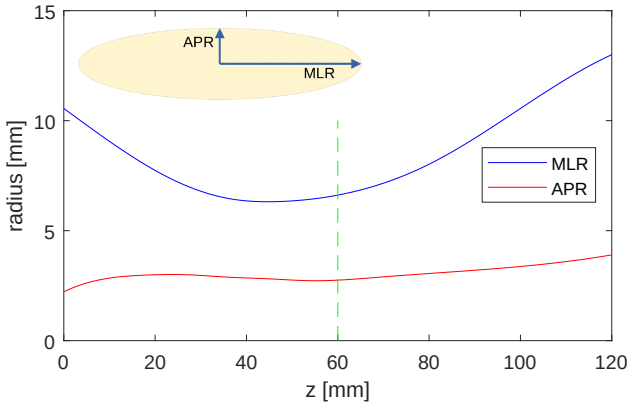

The interior of the ellipses were divided into three main regions, one for each subtendon. They are separated from

Figure 3: Elipsoidal cross section with representation of the internal division for different values of the Z coordinate.

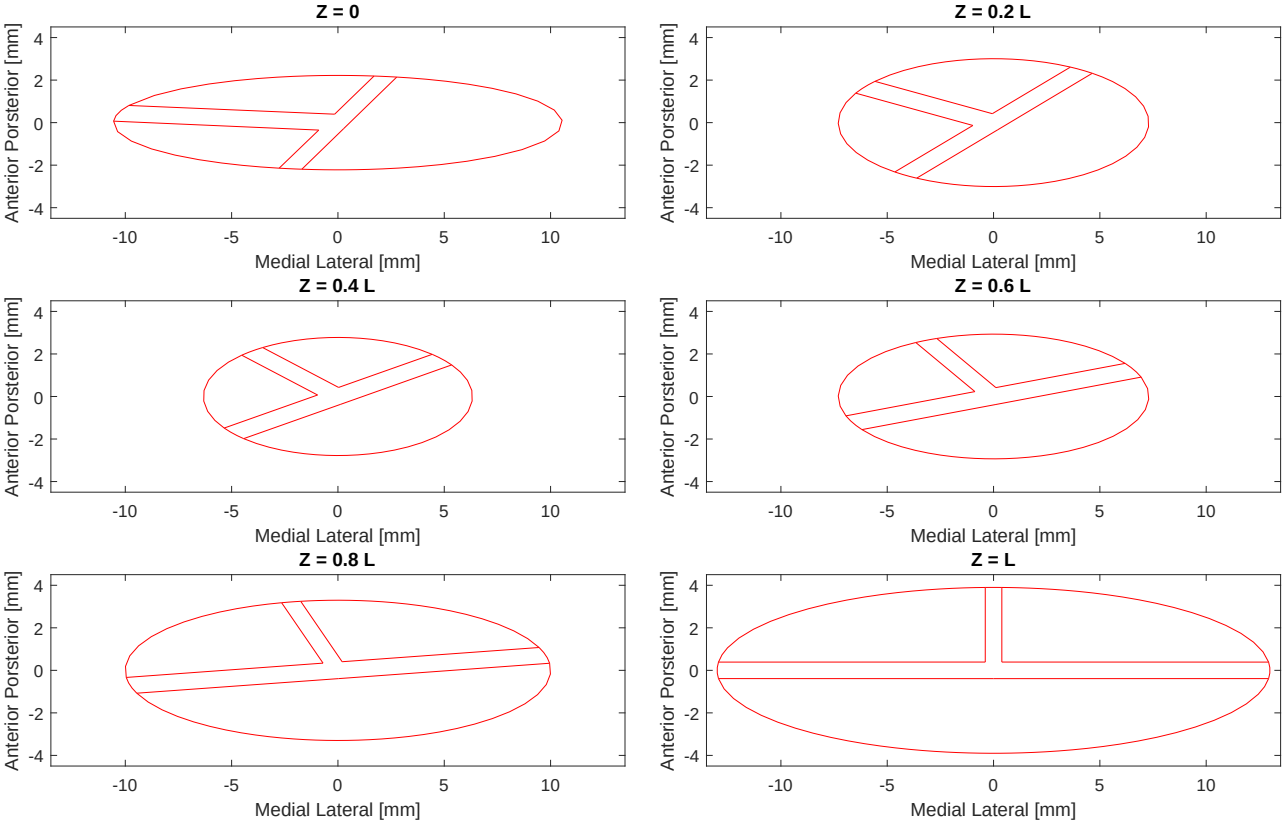

each other by an interface of finite thickness (Figure 3). The relative area fraction of the cross section occupied by each subtendon was keept constant through the whole length of the tendon. The soleus subtendon area fraction was 0.5, while the area fraction of each gastrocnemius subtendon was 0.25.

To represent the internal twist of the subtendons, the internal configuration, but not the principal axis, was rotated gradually in each layer. The rotation was made by rotating the interface portion that separates the soleus and the medial gastrocnemius subtendon (Figure 3). The other interface portions rotated in such a manner as to keep the area fractions unchanged. The rotation followed a variable pitch. The angle varied with the axial position following a quadratic curve.

A cut was made in the distal most portion to represent the bone insertion. The cut formed a surface that makes 30º with the frontal plane.

2.2 Material model

The material model used for the subtendons was the HGO (Gasser *et al.*, 2006), which is defined by the following strain energy potential:

$$U = C_{10}(\bar{I}_1 - 3) + \frac{1}{D}\left(\frac{(J^{el})^2 - 1}{2} - \ln J^{el}\right) + \frac{k_1}{2k_2}\sum_{\alpha=1}^{N}\{\exp\left[k_2\langle\bar{E}_\alpha\rangle^2\right] - 1\}, \tag{1}$$

with

$$\bar{E}_\alpha \overset{\text{def}}{=} \kappa(\bar{I}_1 - 3) + (1 - 3\kappa)(\bar{I}_{4(\alpha\alpha)} - 1), \tag{2}$$

where C_{10}, D, k_1, k_2 and κ are material parameters, $\bar{I}_1$ is the first invariant of the distortional part of the right Cauchy-Green strain ($\bar{C}$), $\bar{I}_{4(\alpha\alpha)}$ is the fourth invariant of the distortional part of the right Cauchy-Green strain ($\bar{C}$) in the direction of the fiber family α, N is the total number of fiber families and J^{el} is the elastic volume ratio.

The HGO material model was chosen due to three main characteristics. 1) It is a transversely isotropic model with an exponential energy function in the fiber directions. 2) The portion of the energy function related to the fiber elastic energy acts only in tension. This characteristic is given by the operator $\langle\cdot\rangle = \frac{1}{2}(|\cdot| + \cdot)$ that basically turns off the energy accumulation of fibers under compression. 3) It is of easy interpretation since by simply considering $\kappa = 0$ one can

readily see that C_{10} and D are analogous to a Neo-Hookean compressible solid and that, for $N = 1$, k_1 and k_2 are the parameters for the exponential energy function of the fiber reinforcement.

For the interface the Neo-Hookean model (Bonet and Wood, 1997), which is defined by the following strain energy potential

$$U = C'_{10}(\bar{I}_1 - 3) + \frac{1}{D'_1}(J_{el} - 1)^2, \tag{3}$$

where C'_{10} and D'_1 are material parameters. The prime symbol ($'$) was used exclusively to differentiate the material parameters of the material model used in the interface from the material parameters of the material model of the subtendons.

2.3 Representation of the tendon as a functionally graded material (FGM)

The material parameters vary with their position in the domain. A scalar predefined field is proposed as a function of position and the material parameters vary as a function of the scalar predefined field. The field was defined analytically as an explicit function of the material coordinates of a point in the domain. The goal is to take into consideration the variation of properties in the Achilles tendon as it gets more proximal and transitions to muscle tissue.

The proposed scalar function has two important values. When $\phi = 0$ it represents muscle tissue and when $\phi = 1$ it represents healthy tendon tissue. When $0 < \phi < 1$ it means the region is partially tendon tissue and partially muscle tissue. The mechanical properties at a given point in the transitions are achieved by interpolation, weighted by the value of ϕ at that point. The function ϕ proposed was

$$\phi = 1 - \frac{|z - l_m| + (z - l_m)}{2(l_0 - l_m)}, \tag{4}$$

where z is the coordinate aligned with the tendon axis, l_m is the value of z above which the tendon is considered to be in the transition region and l_0 is the length of the model at $t = 0$.

The consequence of Equation 4 is that the mechanical properties of the distal half of the model are homogeneous, but in the proximal half ($z \geq l_m$) the material properties changed linearly with the position in the tendon axis to represent the transition from pure tendon tissue to pure muscle tissue.

2.4 Boundary conditions

The distal extremity is formed by a surface with its normal making 30 degrees with the tendon axis. It had all its nodes tied to the movement of a single reference point (RP) and zero displacements and rotations were imposed on its six degrees of freedom. The RP was positioned close to the surface in order to represent the distal bone insertion of the triceps surae MTU.

The proximal extremal face has its nodes separated in four regions, one for each subtendon and one for the interface region. The nodes of each subtendon region were attached to a different reference point and force were imposed on them for the longitudinal direction z (tendon axis) (Figure 4). The displacements were set to zero in the directions perpendicular to the tendon axis, but it was kept free to rotate in all directions. No force were imposed on the interface. The reference points were positioned to simulate the proximal bone insertions of the triceps surae MTU. (Figure 5).

Figure 4: Boundary conditions are associated with reference points (RP) positioned in the proximal insertions of the triceps surae MTU.

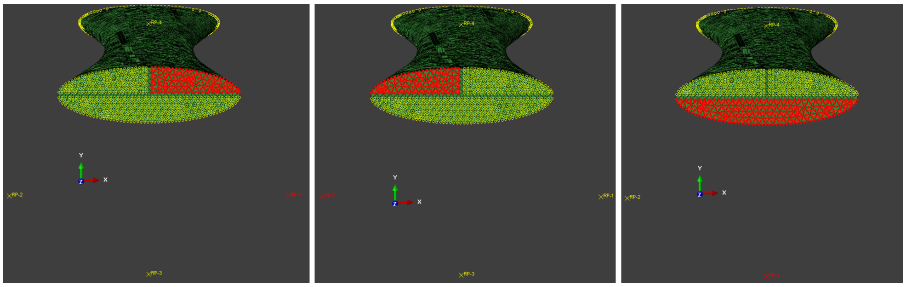

Figure 5: Boundary conditions are associated with reference points (RP) positioned in the proximal insertions of the triceps surae MTU.

3. Validation

3.1 Validation Case 1 - Simple tension test simulation

For this case, the distal reference point was not allowed to either translate or rotate. The proximal reference points were axially loaded, Each of them receiving a fraction of the total force, proportional to the area fraction of the corresponding subtendon. *i.e.* 25% for each gastrocnemius subtendon and 50% for the soleus subtendon. The load value was based on Peltonen *et al.* (2013). The parameters for ϕ were $l_m = 60$ mm and $l_0 = 120$ mm. A set of six different material parameters were tested as shown in Tab.1.

Table 1: Parameters for the material models used for the Validation Case 1.

	Tendon				Muscle				Interface	
	C_{10}	D	k_1	k_2	C_{10}	D	k_1	k_2	C'_{10}	D'
Model 0	10	0.001	60	0.8	1	0.5	6	0.5	0.1	0.01
Model 1	10	0.001	27	0.8	1	0.5	5.4	0.5	0.1	0.01
Model 2	10	0.001	30	0.8	1	0.5	6	0.5	0.1	0.01
Model 3	9	0.001	30	0.8	0.9	0.5	6	0.5	0.1	0.01
Model 4	10	0.001	24	0.8	1	0.5	4.8	0.5	0.1	0.01
Model 5	10	0.001	21	0.8	1	0.5	4.2	0.5	0.1	0.01

3.2 Validation Case 2 - Non uniform load

For this case non uniform load distribution was imposed on the proximal reference points. The distribution followed the experimental tests performed in Lersch *et al.* (2012), which consists on a standard case of load distribution with three load levels, four variations of load distribution and four variations of calcaneal bone rotations.

Table 2: Parameters for the material models used for the Validation Case 2.

	Tendon				Muscle				Interface	
	C_{10}	D	k_1	k_2	C_{10}	D	k_1	k_2	C'_{10}	D'
Model A1	10	0.001	60	0.8	1	0.5	6	0.5	5	0.001
Model A2	10	0.001	24	0.8	1	0.5	4.8	0.5	5	0.001
Model A3	10	0.001	36	0.8	1	0.5	7.2	0.5	5	0.001
Model A4	10	0.001	36	0.8	1	0.5	7.2	0.5	20	0.001
Model A5	10	0.001	36	0.8	1	0.5	7.2	0.5	1.25	0.001
Model A6	10	0.001	36	0.8	1	0.5	7.2	0.5	0.25	0.001

As in Lersch *et al.* (2012), the measurements were made by comparing the distance between different points of the surface at the deformed configuration of each case (L), taking as a reference length (L_{ref}) the distance between the same points when submitted to the first load level. Therefore the strain measurement ($\tilde{\varepsilon}$) is given by

$$\tilde{\varepsilon} = \frac{L - L_{ref}}{L_{ref}}. \tag{5}$$

As a remark, L_{ref} should not be confused with the length of the segment at rest.

Lersch et al. (2012) tested nine load types at three load levels and measured $\tilde{\varepsilon}$ at five different positions for a total of 135 data points per specimen. However, at the second and third load levels, the number of specimens was progressively smaller due to the fact that some specimens failed during the test. Additionally Lersch *et al.* (2012) only informed the maximum and minimum value of $\tilde{\varepsilon}$ for each data point. To work only with experimental data from a fixed sample size the

computational model was compared only with the experimental results from the first load level presented in Lersch *et al.* (2012), totaling 40 data points, 8 load variations (discounting the standard case) with five positions each.

To simplify the comparison of the results of the simulations with the experimental results from Lersch *et al.* (2012) a deviation score is proposed as follows,

$$Ds = \frac{\tilde{\varepsilon}_c - \tilde{\varepsilon}_e}{\Delta\varepsilon_e}, \tag{6}$$

where $\tilde{\varepsilon}_c$ is the measurement of $\tilde{\varepsilon}$ from the computational model, $\tilde{\varepsilon}_e = (\varepsilon_e^{max} + \varepsilon_e^{min})/2$ is the midpoint between the maximum and minimum experimental measurement, ε_e^{max} and ε_e^{min} are the maximum and minimum experimental values of ε presented in Lersch *et al.* (2012) and $\Delta\varepsilon_e = \varepsilon_e^{max} - \varepsilon_e^{min}$. This formulation has as hypothesis that $\tilde{\varepsilon}_e$ represents the exact value of $\tilde{\varepsilon}$ and a minimum or maximal value represents a unitary deviation score for that data point ($Ds = 1$). An ideal result is when all values of Ds equal zero meaning that the model present all its 40 values of $\tilde{\varepsilon}_c = \tilde{\varepsilon}_e$.

To each data point a value for Ds is determined and a mean deviation $\bar{Ds}$ is calculated as

$$\bar{Ds} = \frac{1}{n}\sum_{i=1}^{n} |Ds_i|, \tag{7}$$

where $i = 1...n$ is the identification of the data point ($n = 40$)

4. Results

4.1 Case 1

Six different sets of material properties were tested as presented in Table 1. Resulting in six different force-displacement curves, as can be seen in Figure 6. The displacement measures were taken at the start of the transition region (z=60 mm).

Figure 6: Force-displacement curves for different material properties compared with experimental results from Peltonen *et al.* (2013).

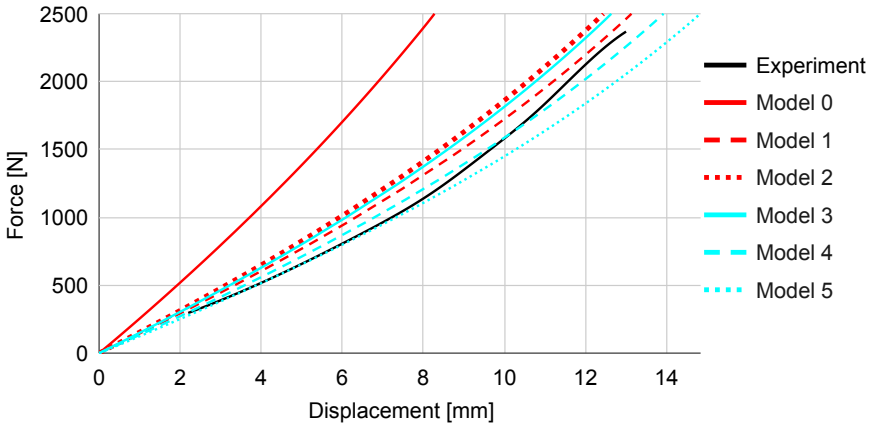

4.2 Case 2

In this case, the relative strain measurements were compared with the results presented in Lersch *et al.* (2012) one by one. To each model set of results a values for $\bar{Ds}$ is shown in Table 3 as explained in subsection 3.2

Table 3: Values of Ds for Case 2.

Model	A1	A2	A3	A4	A5	A6
$\bar{Ds}$	1.45	2.21	1.84	1.73	1.94	1.87

5. Discussion

For the simple tension test it can be seen that the general behaviour was captured with all curves, however, model 0 have not captured the amplitude of the curve. However, experimental data on tendons usually have a quite high dispersion.

Very realistic tests such as the *in vivo* test presented in Peltonen *et al.* (2013) have a standard error of the order of 10% and standard deviation of the order of 30% for stiffness measurements. While *in vitro* tests can present serious boundary conditions issues due to badly planed fixtures as was pointed out in Carniel *et al.* (2019).

The combination of the factors above makes the classical curve fitting for material parameters a inherently limited procedure. The Achilles tendon is not an homogeneous structure and the validation process of a FEM model for it should take it into account.

The comparison made in Case 2 was much richer since each set of material parameters were compared with 40 different measurements. Load variations including uneven muscle activation and calcaneal bone rotation were taken into account as well as non-homogeneity in the displacement field. However, the values obtained for Ds were quite high. The general behaviour of most load variations were satisfactorily captured with the exception of the load variation 3 (Lersch *et al.* (2012)). If load variation 3 was removed from the data set the new table for Ds would improve dramatically (Table 4).

Table 4: Values of Ds for Case 2 assuming that load variation 3 was out of the data set.

Model	A1	A2	A3	A4	A5	A6
Ds	1.07	1.50	1.28	1.21	1.39	1.30

In summary, the model was able to represent the uniaxial behaviour of the Achilles tendon. It was also able to represent most of the inhomogeneities due to calcaneal rotation, uneven muscle load and non negligible shear stresses. The model still require improvements to be considered fully validated.

6. ACKNOWLEDGEMENTS

The authors would like to thank the support of the following agencies: Coordination for the Improvement of Higher Education Personnel (Capes); National Council for Scientific and Technological Development (CNPq); Research Development Foundation of the Federal University of Minas Gerais (Fundep - Grant No.: 29083-144), Brazilian Micro and Small Business Support Service (SEBRAE - Brazil).

Benjamin, M., Theobald, P., Suzuki, D. and Toumi, H., 2007. "The anatomy of the achilles tendon". *The Achilles Tendon*, Vol. 3, pp. 5–16.

Bogaerts, S., Carvalho, C.D.B., Scheys, L., Desloovere, K., D'hooge, J., Maes, F., Suetens, P. and Peers, K., 2017. "Evaluation of tissue displacement and regional strain in the achilles tendon using quantitative high-frequency ultrasound". *PLoS ONE*, Vol. 12. ISSN 19326203. doi:10.1371/journal.pone.0181364.

Bonet, J. and Wood, R.D., 1997. *Nonlinear continuum mechanics for finite element analysis*. Cambridge university press.

Carniel, T.A., Formenton, A.B.K., Klahr, B., Vassoler, J.M., de Mello Roesler, C.R. and Fancello, E.A., 2019. "An experimental and numerical study on the transverse deformations in tensile test of tendons". *Journal of Biomechanics*, Vol. 87, pp. 120–126. ISSN 0021-9290. doi:https://doi.org/10.1016/j.jbiomech.2019.02.028.

Diniz, P., Quental, C., Violindo, P., J., V.G., Pereira, H., Kerkhoffs, G.M.M.J., Ferreira, F.C. and Folgado, J., 2023. "Design and validation of a finite element model of the aponeurotic and free achilles tendon." *J Orthop Res.*, Vol. 41, No. 3, pp. 534–545. doi:10.1002/jor.25408.

Edama, M., Kubo, M., Onishi, H., Takabayashi, T., Inai, T., Yokoyama, E., Hiroshi, W., Satoshi, N. and Kageyama, I., 2015. "The twisted structure of the human achilles tendon". *Scandinavian Journal of Medicine and Science in Sports*, Vol. 25, pp. e497–e503. ISSN 16000838. doi:10.1111/sms.12342.

Edama, M., Kubo, M., Onishi, H., Takabayashi, T., Yokoyama, E., Inai, T., Watanabe, H., Nashimoto, S. and Kageyama, I., 2016. "Structure of the achilles tendon at the insertion on the calcaneal tuberosity". *Journal of Anatomy*, Vol. 229, pp. 610–614. ISSN 14697580. doi:10.1111/joa.12514.

Gasser, T., Ogden, R. and Holzapfel, G., 2006. "Hyperelastic modelling of arterial layers with distributed collagen fibre orientations". *J R Soc Interface*, Vol. 22, pp. 15–35. doi:10.1098/rsif.2005.0073.

Handsfield, G.G., Inouye, J.M., Slane, L.C., Thelen, D.G., Miller, G.W. and Blemker, S.S., 2017. "A 3d model of the achilles tendon to determine the mechanisms underlying nonuniform tendon displacements". *Journal of Biomechanics*, Vol. 51, pp. 17–25. ISSN 18732380. doi:10.1016/j.jbiomech.2016.11.062.

Lersch, C., Grötsch, A., Segesser, B., Koebke, J., Brüggemann, G.P. and Potthast, W., 2012. "Influence of calcaneus angle and muscle forces on strain distribution in the human achilles tendon". *Clinical Biomechanics*, Vol. 27, pp. 955–961.

Maganaris, C.N., Narici, M.V. and Almekinders, L. C. Maffulli, N., 2004. "Biomechanics and pathophysiology of overuse tendon injuries: ideas on insertional tendinopathy." *Sports Med.*, Vol. 34(14), pp. 1005–17.

Obrezkov, L.P., Finni, T. and Matikainen, M.K., 2022. "Modeling of the achilles subtendons and their interactions in a framework of the absolute nodal coordinate formulation". *Materials*, Vol. 15, No. 24. ISSN 1996-1944. doi: 10.3390/ma15248906.

Obst, S.J., Renault, J.B., Newsham-West, R. and Barrett, R.S., 2014. "Three-dimensional deformation and transverse rotation of the human free achilles tendon in vivo during isometric plantarflexion contraction." *J Appl Physiol (1985).*, Vol. 116(4), pp. 376–84.

Oliva, F., Via, A. and Maffulli, N., 2012. "Physiopathology of intratendinous calcific deposition." *BMC Med 10*, Vol. 95.

Pekala, P.A., Henry, B.M., Ochala, A., Kopacz, P., Taton, G., Mlyniec, A., Walocha, J.A. and Tomaszewski, K.A., 2017. "The twisted structure of the achilles tendon unraveled: A detailed quantitative and qualitative anatomical investigation". *Scandinavian Journal of Medicine and Science in Sports*, Vol. 27, pp. 1705–1715. ISSN 16000838. doi:10.1111/sms.12835.

Peltonen, J., Cronin, N.J., Stenroth, L., Finni, T. and J., A., 2013. "Viscoelastic properties of the achilles tendon in vivo". *Springerplus*, Vol. 2. doi:10.1186/2193-1801-2-212.

Prosenz, J., Rath, C., Hadrovic-Avdic, M. and Hirtler, L., 2018. "The twist of the achilles tendon - associations of torsions in the lower extremity". *Clin Anat*, Vol. 31, pp. 1085–1091.

Shim, V.B., Hansen, W., Newsham-West, R., Nuri, L., Obst, S., Pizzolato, C., Lloyd, D.G. and Barrett, R.S., 2019. "Influence of altered geometry and material properties on tissue stress distribution under load in tendinopathic achilles tendons - a subject-specific finite element analysis." *J Biomech.*, Vol. 82, pp. 142–148.

Shim, V.B., Fernandez, J.W., Gamage, P.B., Regnery, C., Smith, D.W., Gardiner, B.S., Lloyd, D.G. and Besier, T.F., 2014. "Subject-specific finite element analysis to characterize the influence of geometry and material properties in achilles tendon rupture". *Journal of Biomechanics*, Vol. 47, pp. 3598–3604. ISSN 18732380. doi: 10.1016/j.jbiomech.2014.10.001.

Shim, V.B., Handsfield, G.G., Fernandez, J.W., Lloyd, D.G. and Besier, T.F., 2018. "Combining in silico and in vitro experiments to characterize the role of fascicle twist in the achilles tendon". *Scientific Reports*, Vol. 8, pp. 1–12.

Szaro, P., Ramirez, W.C., Borkmann, S., Bengtsson, A., Polaczek, M. and Ciszek, B., 2020. "Distribution of the subtendons in the midportion of the achilles tendon revealed in vivo on mri". *Scientific Reports*, Vol. 10. ISSN 20452322. doi:10.1038/s41598-020-73345-0.

Yin, N.H., Fromme, P., McCarthy, I. and Birch, H.L., 2021a. "Individual variation in achilles tendon morphology and geometry changes susceptibility to injury". *eLife*, Vol. 10, pp. 1–15. ISSN 2050084X. doi:10.7554/eLife.63204.

Yin, N.H., Fromme, P., McCarthy, I. and Birch, H.L., 2021b. "Individual variation in achilles tendon morphology and geometry changes susceptibility to injury". *eLife*, Vol. 10, p. e63204. ISSN 2050-084X. doi:10.7554/eLife.63204.

7. RESPONSIBILITY NOTICE

The authors are the only responsible for the printed material included in this paper.